

The British University in Egypt

**BUE Scholar**

---

Nanotechnology Research Centre

Research Centres

---

5-24-2023

## Synthesis and Functional Properties of La<sub>2</sub>FeCrO<sub>6</sub> Based Nanostructures

Mohamed Morsy

mohamed.morsy@bue.edu.eg

Follow this and additional works at: [https://buescholar.bue.edu.eg/nanotech\\_research\\_centre](https://buescholar.bue.edu.eg/nanotech_research_centre)

 Part of the [Condensed Matter Physics Commons](#)

---

### Recommended Citation

Morsy, Mohamed, "Synthesis and Functional Properties of La<sub>2</sub>FeCrO<sub>6</sub> Based Nanostructures" (2023). *Nanotechnology Research Centre*. 54.

[https://buescholar.bue.edu.eg/nanotech\\_research\\_centre/54](https://buescholar.bue.edu.eg/nanotech_research_centre/54)

This Article is brought to you for free and open access by the Research Centres at BUE Scholar. It has been accepted for inclusion in Nanotechnology Research Centre by an authorized administrator of BUE Scholar. For more information, please contact [bue.scholar@gmail.com](mailto:bue.scholar@gmail.com).



# Synthesis and Functional Properties of $\text{La}_2\text{FeCrO}_6$ Based Nanostructures

Ebtesam E. Ateia<sup>1</sup> · D. Gawad<sup>1</sup> · Mohamed Mosry<sup>2,3</sup> · M. M. Arman<sup>1</sup>

Received: 24 March 2023 / Accepted: 4 May 2023  
© The Author(s) 2023

## Abstract

Ordered double perovskite  $\text{La}_2\text{FeCrO}_6$  nanoparticles (NPs) were synthesized via the citrate auto-combustion technique. The prepared sample was characterized by X-ray diffraction (XRD), energy dispersive X-ray analysis (EDAX), and Raman spectroscopy, which confirmed the double perovskite structure of the studied sample. XRD illustrated that the investigated sample has an orthorhombic structure with an average crystallite size of 25.3 nm.  $\text{La}_2\text{FeCrO}_6$  NPs exhibit a porous structure and spongy morphology, as determined through analyses using Brunauer–Emmett–Teller (BET) specific surface area and field emission scanning electron microscopy (FESEM). The studied sample exhibits anti-ferromagnetic (AFM) behavior with weak ferromagnetic (FM) components, as an example of  $d^5(\text{Fe}^{3+})-d^3(\text{Cr}^{3+})$  systems. The AFM behavior is caused by the super-exchange interaction between  $[\text{Fe}^{3+}(d^5)-\text{O}-\text{Cr}^{3+}(d^3)]$ , according to the Kanamori–Goodenough (KG) rule. This behavior is induced by the  $pd\pi$  hybridization between the  $e_g$  orbital of the transition metal and the  $p\sigma$  orbital of the oxygen, while the one induced by the  $pd\sigma$  hybridization is FM. The number of excited-state configurations mediated by the  $pd\pi$  hybridization in the Fe–Cr pair is greater than that mediated by  $pd\sigma$  hybridization. Pb(II) heavy metal ions are used in adsorption studies. The electrostatic nature of the bonding between Pb(II) and the  $\text{La}_2\text{FeCrO}_6$  nano ferrite sample is thought to be the main cause of the observed high sorption of  $\text{La}_2\text{FeCrO}_6$  to a Pb(II) ion.  $\text{La}_2\text{FeCrO}_6$  has a favorable morphology, which bodes well for its prospective applications in Li-ion batteries, water purification, and gas sensors.

**Keywords** Double perovskite · Antiferromagnetic feature · Super exchange interaction · Citrate auto-combustion · Heavy metal removal

## 1 Introduction

The double-perovskite (DPV) compound  $\text{A}_2\text{B}'\text{B}''\text{O}_6$  offers a versatile framework for engineering materials with untapped magnetic and electronic properties [1].

DPV obtained considerable attention and importance due to its potential applications: the magnetic memories [2, 3],

the tunnel junctions [4], the spintronic field [5, 6], the microwave, and the high-power applications [7–9].

Furthermore, this class of materials displays numerous fascinating physical and chemical characteristics, including electronic structures that range from insulating to metallic, and half-metallic spin-polarized electrical conductivity [10, 11].

DPVs include perovskites with two different kinds of cations occupying the A or B sites, resulting in the formulae  $\text{A}_2\text{B}'\text{B}''\text{O}_6$  (A is a rare earth and/or an alkaline-earth metal, and B' and B'' are d-block transition metals) that exhibit naturally well-ordered structures:  $\text{B}'\text{O}_6$  and  $\text{B}''\text{O}_6$  octahedrons with FCC-NaCl sublattice arrangement [12].

DPVs are typically denoted as double B-site perovskites because A-site cations typically serve as electron donors to the  $[\text{BO}_6]$  framework. The ordering of various types of  $\text{BO}_6$  octahedrons is influenced by the presence of a sizable difference in the ionic radii and formal valence between B' and B'' ions.

✉ Ebtesam E. Ateia  
drebtesam2000@yahoo.com; ebtesam@sci.cu.edu.eg

<sup>1</sup> Physics Department, Faculty of Science, Cairo University, Giza, Egypt

<sup>2</sup> Building Physics and Environment Institute, Housing & Building National Research Center (HBRC), Dokki, Giza 12311, Egypt

<sup>3</sup> Nanotechnology Research Centre (NTRC), The British University in Egypt (BUE), Suez Desert Road, El-Sherouk City, Cairo 11837, Egypt

This ordering can be complete or partial, depending on the charge and the difference in the ionic radius of the two cations. The degree of ordering tends to increase with increasing size and charge differences.

On the other hand, it is challenging to construct ordered structures when the ionic radii of two types of transition metal elements are nearly identical. All these factors involving the crystal structure, lattice defect, exposed lattice plane, surface morphology, particle size, specific surface area, and pore structure highly affect the physicochemical characteristics of the DPV materials.

In the  $A_2B'B''O_6$  structures, the d-block elements are considered promising candidates for filling up the B-site cation position because of their multi-valence state and the unique  $3d$  and  $4d$  electronic configurations. This is the real cause of the perovskite-like structures found in transition metal oxides, and they frequently have exceptional physical properties [13]. Because of the large difference in atomic radius between  $B'$  and  $B''$ , it is simple to synthesize a well-ordered DPV containing the combination of  $B'$  of a 3D element and  $B''$  of a 4D or 5D element [14–17]. Some DPV compounds in this category have a Curie Temperature  $T_c$  above the room temperature, such as  $Sr_2FeMoO_6$  and  $Sr_2FeReO_6$  [18]. According to K. Miura et al. [17], for  $La_2FeCrO_6$ , the majority-spin  $t_{2g}$  states of the Cr ions (HOMO) are below the Fermi level, while the minority-spin  $t_{2g}$  states of the Fe ions (LUMO) are above the Fermi level, which controls the constancy of the magnetic ordering.

In the present work, the  $La_2FeCrO_6$  is prepared via the citrate auto-combustion technique, which is characterized by simplicity, low cost, and no waste. The structural, morphological, and magnetic properties of the sample are studied. The application of heavy metal ( $Pb^{2+}$ ) removal from waste water is given in the current work. The Langmuir and Freundlich isotherms for ad-sorption will be discussed.

## 2 Experimental Work

### 2.1 Materials

$La(NO_3)_3 \cdot 6H_2O$ ,  $Fe(NO_3)_3 \cdot 9H_2O$ ,  $Cr(NO_3)_3 \cdot 9H_2O$ , and citric acid with high purity (99.999%) were employed as preliminary ingredients. All the utilized raw materials were provided by ACROS Organics Company in the UK.

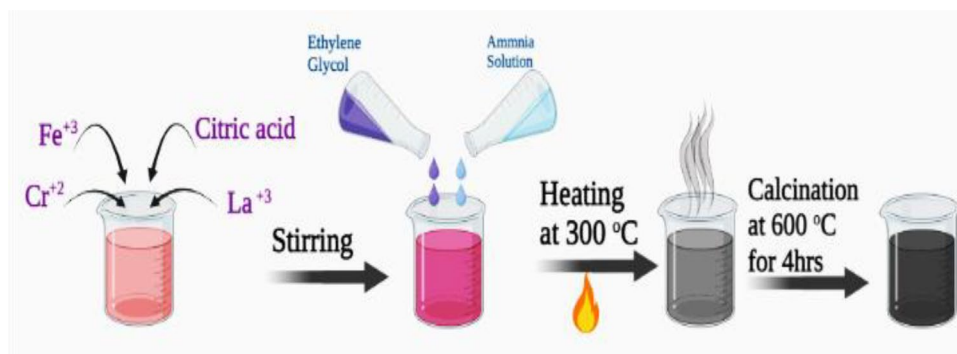
### 2.2 Synthesis of $La_2FeCrO_6$ NPs

The preparation method is demonstrated through the schematic diagram shown in Fig. 1, as mentioned in the previous work [15].

### 2.3 Characterization Techniques

X-ray powder diffraction pattern was used to determine the XRD of the produced sample.  $Cu-K\alpha$  radiation having a wavelength of 0.1542 nm was produced using a Cu X-ray tube (line source of  $12 \times 0.04 \text{ mm}^2$ ) (Netherlands-based X'Pert PRO Analytical). With the aid of High Score Plus software, it was run at 45 kV. By employing a SEM Model Quanta 250 FEG coupled with an EDAX unit, FESEM was used to examine the morphology and nanostructure of the materials. A VSM, Model Lake Shore 7410, was used to assess the sample's magnetic characteristics. The magnetization in emu/g was measured as a function of magnetic field intensity at a temperature of 300 K. The Raman measurements were performed with a Senterra-Bruker (Germany) instrument and a laser source (ND:YAG) at 532 nm. The BET technique [19] was used to calculate the specific surface area based on nitrogen ad-sorption and de-sorption isotherms at 77 K, which were acquired using a NOVA 2200, USA, together with an automated gas sorption system. The three-dimensional atomic force microscopy (AFM) pictures produced by a 5600 LS AFM provided complementary details regarding the surface microstructure of the sample under investigation.

**Fig. 1** Schematic representation of the citrate auto-combustion method



## 2.4 Heavy Metal Removal

On the way to investigating the effectiveness of  $\text{La}_2\text{FeCrO}_6$  in removing heavy metal ions, a solution of lead ( $\text{Pb}^{2+}$ ) ions of the necessary concentration (50 ppm) was prepared and placed in a beaker containing an amount of 0.10 g of  $\text{La}_2\text{FeCrO}_6$ . The optimal value of pH is adjusted well at pH 7. The concentration of  $\text{Pb}^{2+}$  present in the solution was determined in the filtrate by using inductively coupled plasma (ICP) spectrometry (Prodigy7).

The ad-sorption capacity at equilibrium ( $q_e$ ) and the efficiency of metal ion removal were determined using the following equation [20]:

$$\eta = \frac{C_i - C_e}{C_i} \times 100 \quad (1)$$

$$q_e = \frac{(C_i - C_e)V}{m} \quad (2)$$

The concentrations of a metal ion solution, expressed in mg/L, are represented by  $C_i$  and  $C_e$ , where  $C_i$  is the initial concentration and  $C_e$  is the final concentration. The mass of the adsorbent is represented by  $m$ , while the volume of the  $\text{Pb}(\text{II})$  solution is represented by  $V$ .

## 3 Results and Discussion

### 3.1 XRD Analysis

The XRD of  $\text{La}_2\text{CrFeO}_6$  presented in Fig. 2 demonstrates eight sharp diffraction peaks. The peak positions at  $2\theta$  of  $22.76^\circ$ ,  $32.39^\circ$ ,  $39.98^\circ$ ,  $46.44^\circ$ ,  $52.3^\circ$ ,  $57.74^\circ$ ,  $67.78^\circ$ , and  $77.13^\circ$  can be indexed to (110), (112), (022), (220), (222), (204), (224), and (332) diffraction planes of the orthorhombic  $\text{La}_2\text{CrFeO}_6$  space group  $Fmm2$ . It coincides with card No. 00-056-0263. The pattern exhibits broad peaks with no evidence for other impurities. The Scherrer equation is applied, as stated in earlier studies [21, 22], to calculate the crystallite size of  $\text{La}_2\text{CrFeO}_6$ .

The crystallite size, as determined through calculation, is 23.3 nm, which confirms the nanoscale size of the investigated sample. The lattice parameters are calculated on the basis of the orthorhombic structure and are listed in Table 1.

It is very important to perform some additional calculations to get a closer look at the crystal structure of the  $\text{La}_2\text{CrFeO}_6$  composite. The XRD diffraction pattern can reveal some information regarding, the tolerance factor (T) [24], the theoretical density ( $d_x$ ) [25, 26], dislocation density ( $\delta$ ) [27, 28], the micro strain ( $\epsilon$ ) [29], and the degree of crystallinity ( $X_c$ ). The experimental density ( $D_{ex}$ ) of the sample is calculated according to the following equation:

$$D_{ex} = \frac{m}{V} \quad (3)$$

where  $m$  and  $V$  are the mass and volume of the pellet sample, respectively. The value of  $D_{ex}$  is reported in the Table.

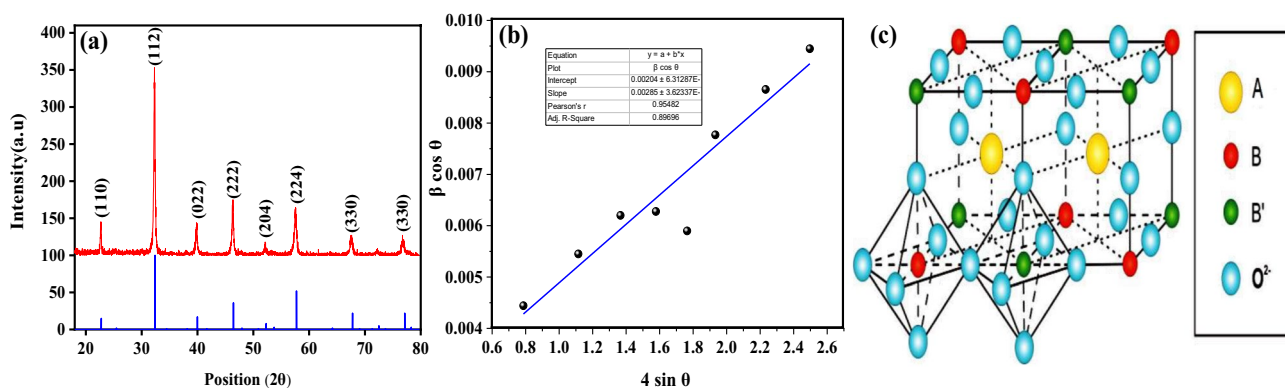


**Fig. 2** a X-ray diffraction pattern; b the W–H plot of  $\text{La}_2\text{CrFeO}_6$  sample; and c the crystal structure of double perovskite [23]

**Table 1** Lattice parameters (a, b and c), crystallite size from Scherrer equation (L), crystallite size (D) from W–H, micro strain ( $\epsilon$ ), tolerance factor (T), theoretical density ( $d_x$ ), experimental density ( $D_{exp}$ ), dislocation density ( $\delta$ ), and degree of crystallinity ( $X_c$ )

Sample	Lattice parameter (Å)	L (nm)	D (nm)	$\epsilon \times 10^{-3}$	T	$d_x$ (g/cm <sup>3</sup> )	$D_{exp}$ (g/cm <sup>3</sup> )	$\delta \times 10^{-3}$ (nm <sup>-2</sup> )	$X_c$
$\text{La}_2\text{FeCrO}_6$	a = 5.126, b = 5.533, and c = 7.973	22.61	23.32	2.74	0.959	7.07	2.96	2	98.5%

The difference between the theoretical and experimental densities is due to the porous nature of the sample. The porosity (P) of the investigated sample is calculated from the following equation [30] and equals 58.13%.

$$P\% = \left(1 - \frac{D_{exp.}}{d_x}\right) \times 100 \quad (4)$$

It's well known that the Scherrer equation omits the intrinsic strain that emerged in the nanocrystals as a result of point defects, grain boundaries, or any defect that generates an alternation of the sequence periodicity of the layers.

The Williamsons Hall (W–H) method is a straightforward technique for determining the size of crystal structures and estimating any deformation in the lattice structure using Eq. 5, as mentioned in the previous work [31].

$$\beta \cos \theta = \frac{K\lambda}{D} + 4\epsilon \sin \theta \quad (5)$$

where the broadening of the XRD peak is caused by the size ( $\beta_{size}$ ). This relation represents a simple straight line with good fitting, as shown in Fig. 2b. The crystallite size (D) can be obtained from the y-axis intercept, while  $\epsilon$  is calculated from the slope of the line [32]. The calculated D and  $\epsilon$  are tabulated in Table 1.

The degree of crystallinity ( $X_c$ ) is estimated from the area underneath the crystalline peaks divided by the total area under the crystalline and non-crystalline peaks, as expressed by the following equation:

$$X_C = \frac{X_{Cry}}{X_{all}} \times 100 \quad (6)$$

The degree of crystallinity is found to be 98.5%.

The calculation of the tolerance factor (T) is performed using the well-known Goldschmidt relation [33]. The value of the 'T' for the investigated sample is 0.959, which indicates an orthorhombic structure. However, the B' and B'' elements in the compound are evenly balanced with transition metals, with an oxygen ion placed symmetrically between each pair as shown in Fig. 2c. If B' and B'' differ from each other, the O<sup>2-</sup> ions move somewhat in either charges or ionic

radii, as in the example that is currently being discussed, while the B'O<sub>6</sub> and B''O<sub>6</sub> retain their octahedral symmetry. Along with the newly discovered structure, two non-equivalent O<sub>2</sub> atoms (O<sub>1</sub>, O<sub>2</sub>) are also present. Four O<sub>2</sub> atoms are placed on the XY plane, while the two O<sub>1</sub> atoms are situated on the Z axis. Contrarily, in a structure with differently bonded oxygen atoms, the angle between B'–O<sub>1</sub>–B'' remains fixed at 180°, while the angle between B'–O<sub>2</sub>–B'' may vary. The c/a ratio during structural optimization is extremely close to the value of  $\approx \sqrt{2}$ . This situation gives rise to the anti-ferromagnetic characteristic, as will be discussed in detail later.

### 3.2 FE-SEM

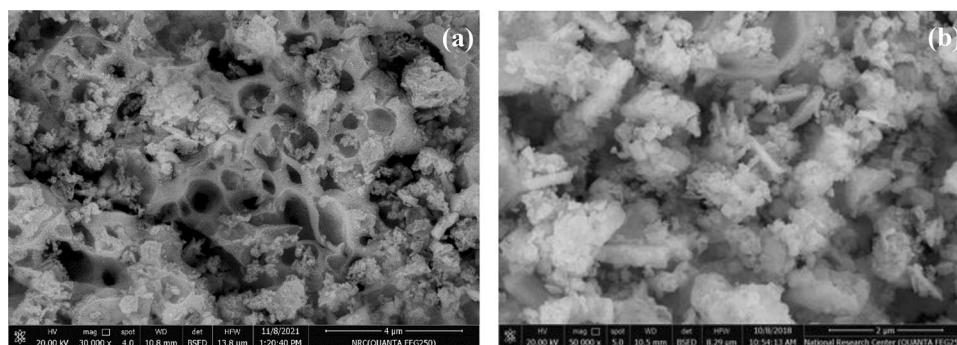
The morphologies of the investigated sample, La<sub>2</sub>FeCrO<sub>6</sub>, are studied by FESEM, as illustrated in Fig. 3. The La<sub>2</sub>FeCrO<sub>6</sub> NPS have a sponge-like morphology. As shown in the figure, the studied sample as they are formed, have pores and voids that depend on a lot of gases during the burning process. La<sub>2</sub>FeCrO<sub>6</sub> has a favorable morphology, which bodes well for its prospective application in Li-ion batteries, water purification, and gas sensors.

### 3.3 EDAX Mapping

The EDAX cation mapping of La<sub>2</sub>FeCrO<sub>6</sub> is shown in Fig. 4a–e. The homogeneous distribution of the cations (La, Fe, Cr, and O) is observed in the mapping images with different colors. The mapping shows the uniformity of the distribution of the constituent elements throughout the sample matrix.

The pattern displayed in Fig. 5 is obtained through an EDAX analysis of the studied sample [34]. The figure displays the presence of the starting chemical composition without any impurities. The theoretical atomic-percentage (at%) and theoretical weight-percentage (wt%) of the elements (La, Cr, Fe and O) are calculated from the chemical composition La<sub>2</sub>FeCrO<sub>6</sub>. Table 2 displays both the atomic percentage (at%) and weight percentage (wt%) obtained

**Fig. 3** a and b FESEM images for La<sub>2</sub>FeCrO<sub>6</sub>



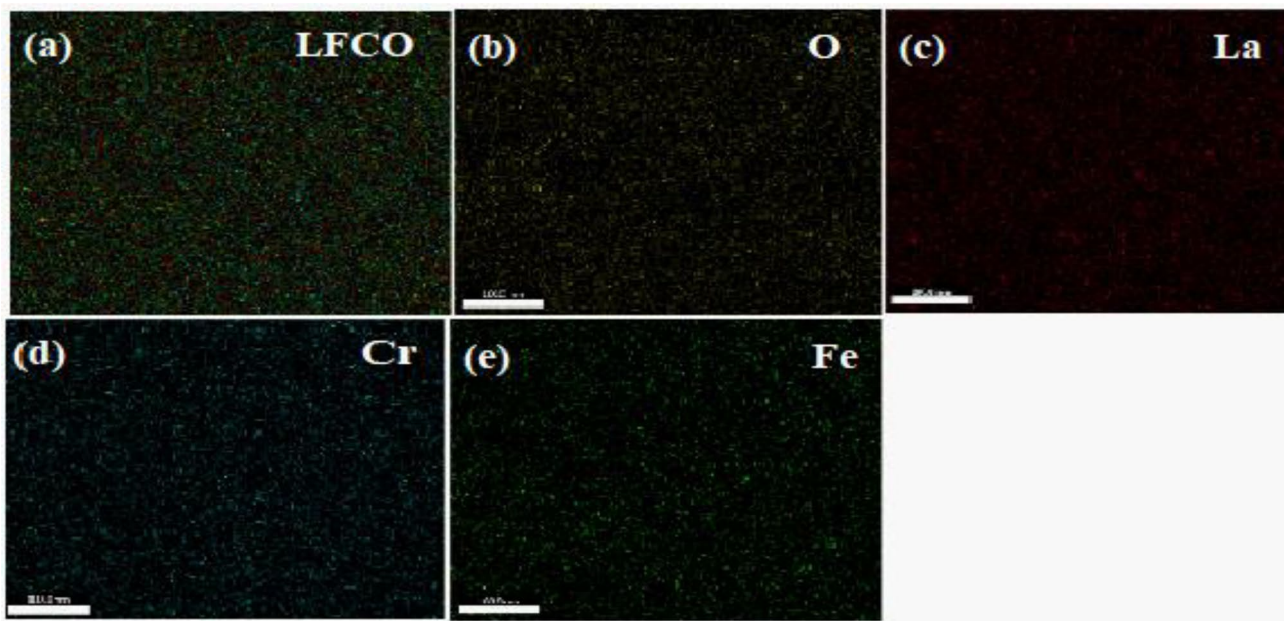


Fig. 4 a–e The elemental mapping images for  $\text{La}_2\text{FeCrO}_6$

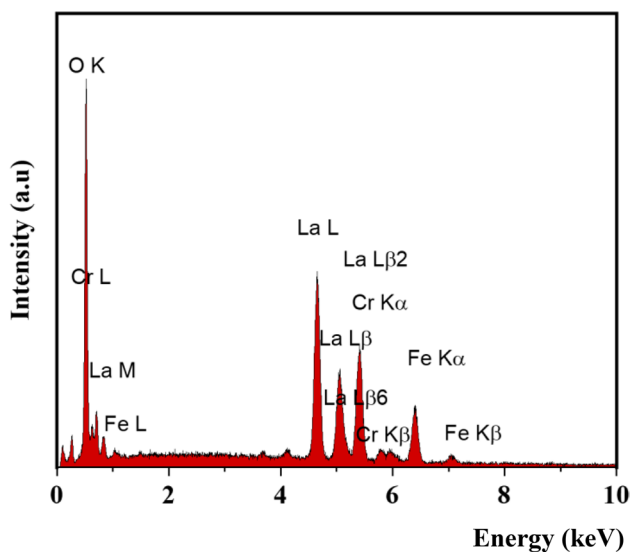


Fig. 5 Illustrates EDAX pattern for  $\text{La}_2\text{FeCrO}_6$

**Table 2** The expected and experimental values of the atomic percentage (at.%) and weight percentage (wt%) for the sample

Elements	Expected weight%	Exp. weight%	Expected atomic%	Exp. atomic%
O K	19.94	25.99	60	66.85
La L	57.68	50.13	20	14.85
Cr K	10.79	12.94	10	10.24
Fe K	11.59	10.94	10	8.06
Total %	100%	100%	100%	100%

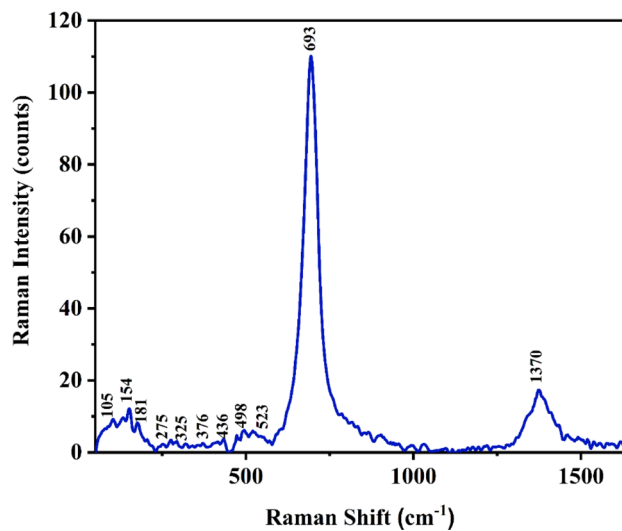


Fig. 6 Raman spectrum of  $\text{La}_2\text{FeCrO}_6$

through EDAX elemental analysis, as well as those calculated theoretically.

### 3.4 Raman Spectroscopy (RS)

RS is extensively used for several lattice vibrational modes that are strongly related to the local crystal structure. Figure 6 displays the vibrational modes detected in the  $\text{La}_2\text{FeCrO}_6$  NPs that originate from Fe/CrO<sub>6</sub> octahedra and La–O bonds, in addition to the presence of coupling between

them. The Raman peaks are observed at 105, 154, 181, 275, 325, 376, 436, 498, 523, 693, and  $1370\text{ cm}^{-1}$ . The peaks can be divided into four regimes based on their characteristics.

The lowest wave number modes below  $200\text{ cm}^{-1}$  can be assigned to the translational motion of the rare-earth element (La), which is coupled to the tilting vibrations of the Fe/CrO<sub>6</sub> octahedron and labelled as (A) [35–37].

In the frequency regime ( $200\text{--}350\text{ cm}^{-1}$ ) [38], the peaks correspond to the A site and different tilt modes of the octahedral oxygen (T). The Raman peaks that arise in the regime

( $350\text{--}500\text{ cm}^{-1}$ ) are due to Fe/CrO<sub>6</sub> octahedra bending modes and labelled as (B). The presence of stretching vibrations of oxygen can be identified in the Raman region above  $500\text{ cm}^{-1}$  (S) [36]. The strongest intense peak at  $693\text{ cm}^{-1}$  can be ascribed to the oxygen stretching modes in Fe/CrO<sub>6</sub> octahedra. It is improved by the photon induced transfer of an electron from a Fe<sup>3+</sup> ion to a nearby Cr<sup>3+</sup> ion, owing to the mixed tendency of the metal cations [37, 38].

In addition to the above modes, there is a high-frequency broad peak at  $1370\text{ cm}^{-1}$ , which is positioned at an energy value slightly lower than twice that of the first order mode. This peak is considered an overtone mode of the fundamental stretching mode [39]. The Raman modes of the investigated sample, La<sub>2</sub>FeCrO<sub>6</sub>, are listed in Table 3.

**Table 3** The Raman modes of LFCO sample

Mode labels	Raman modes	La <sub>2</sub> Fe-CrO <sub>6</sub> (cm <sup>-1</sup> )
A ( $100\text{--}200\text{ cm}^{-1}$ ) (La-O, M-O)	B <sub>1g</sub> A <sub>g</sub>	154 181
T ( $200\text{--}350\text{ cm}^{-1}$ ) (MO <sub>6</sub> )	A <sub>g</sub>	275 325
B ( $350\text{--}500\text{ cm}^{-1}$ ) (MO <sub>6</sub> )/O-M-O	B <sub>3g</sub> A <sub>g</sub>	436 498
S (above $500\text{ cm}^{-1}$ ) (M-O)	B <sub>2g</sub>	693

### 3.5 Atomic Force Microscopy (AFM)

The topographic features of the nanocrystalline DPV are characterized using the AFM. Characteristic AFM micrographs of the sample are displayed in Fig. 7a–c. The parameters of the surface profile can be divided into four categories: amplitude, spacing, hybrid, and functional.

Firstly, the amplitude or height parameters, which are the principal parameters in characterizing the surface's

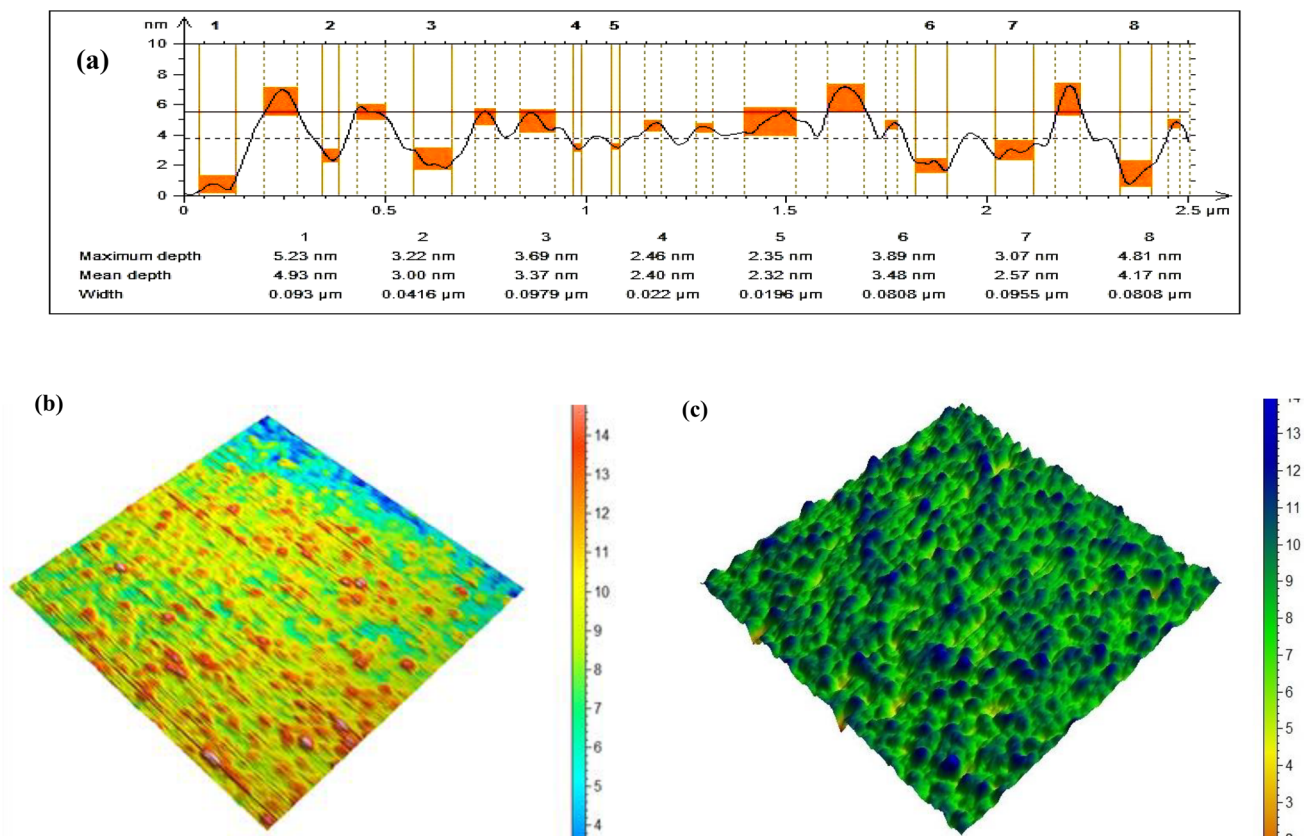


**Fig. 7** a–c Different AFM images of LaFCO: **a** 2D- AFM image. **b** 3D-AFM image. **c** AFM imaging topography

topography and include:  $R_p$ , the maximum profile peak height relative to the mean line,  $R_v$ , the lowest point of the deepest valley compared to the average line,  $R_T$ , the total roughness,  $R_a$ , the average roughness,  $R_q$ , the root mean square (RMS) of roughness.

Secondly, the functional or statistical parameters that provide information about the structure of the investigated surface are the skewness ( $R_{sk}$ ) and kurtosis ( $R_{ku}$ ) moments that determine the asymmetry and the sharpness, respectively. For bumpy surfaces,  $R_{ku} < 3$ , while for spiky surfaces,  $R_{ku} > 3$ . According to the value of  $R_{ku}$ , the  $\text{La}_2\text{FeCrO}_6$  sample has a bumpy surface ( $R_{ku} = 2.69$ ) that matches well with the porous structure seen in FESEM.

Thirdly, hybrid parameters that show quantitatively the spacing features of the surface as  $\Delta_q$ , as well as the RMS of the mean profile slope that is taken between each two successive points of the profile. Finally, the spacing parameters like  $S_m$ , the average spacing of adjacent local peaks in the profile. Table 4 shows the measured values of the mentioned above parameters as provided by AFM.

### 3.6 Brunauer–Emmett–Teller (BET) Technique

The  $\text{N}_2$  ad-sorption-de-sorption isotherms of  $\text{La}_2\text{FeCrO}_6$  are shown in Fig. 8. It is obvious that ad-sorption/de-sorption curves show a hysteresis feature characteristic of mesoporous structures [40, 41]. According to the International Union of

Pure and Applied Chemistry (IUPAC) classifications [42], the (Ads/Des)-isotherm is classified as IV category.

The behavior of ad-sorption of  $\text{N}_2$  gas molecules depends on the relative pressure, such that, in regions of lower pressure, the formation of a monolayer is followed by the formation of multilayers of the ad-sorbed molecules in the regions of higher pressure.

Materials with slit-shaped pores and no limiting ad-sorption at high  $P/P_0$  are classified as type H3. In the present case, the IV category is classified according to the form of the hysteresis loop and the texture (e.g., pore size distribution, pore geometry, and connectivity) as type H3.

Figure 8.b shows the distribution of pore radius against pore volume for the investigated sample. The maximum peak indicates the average value of the pore radius, which has a good impact on  $\text{Pb}^{2+}$  removal efficiency, as will be discussed later.

BET isotherms and BET multipoint plots are performed for the determination of the average values of specific surface area ( $S_{\text{BET}}$ ), pore size, and total pore volume of  $\text{La}_2\text{FeCrO}_6$  NPs, as reported in Table 5.

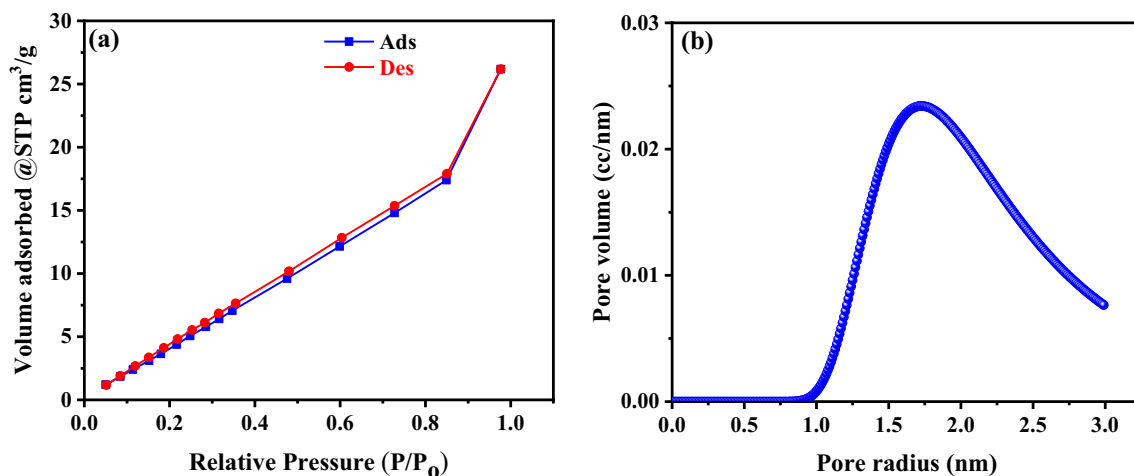
### 3.7 Magnetic Properties

Figure 9a illustrates the magnetic hysteresis loop (MHL) for the  $\text{La}_2\text{FeCrO}_6$  NPs. Because  $\text{Fe}^{3+}$  ( $r = 0.645 \text{ \AA}$ ) and  $\text{Cr}^{3+}$  ( $r = 0.615 \text{ \AA}$ ) have the same valence state and closer ionic

**Table 4** Maximum profile peak height ( $R_p$ ), maximum profile valley depth ( $R_v$ ), maximum height of the profile ( $R_T$ ), average roughness ( $R_a$ ), root mean square roughness ( $R_q$ ), skewness of the line

Sample	$R_p$ (nm)	$R_v$ (nm)	$R_T$ (nm)	$R_a$ (nm)	$R_q$ (nm)	$R_{sk}$	$R_{ku}$	$\Delta_q$	$S_m$ ( $\mu\text{m}$ )
LFCO	2.38	1.91	4.30	0.77	0.96	0.26	2.69	2.13	0.286

( $R_{sk}$ ), and kurtosis of the line ( $R_{ku}$ ), root mean square of the mean profile slope  $\Delta_q$ , the average spacing ( $S_m$ )



**Fig. 8** a, b Type of ad-sorption/de-sorption isotherms and pore size distribution of  $\text{La}_2\text{FeCrO}_6$

**Table 5** The specific surface area ( $S_{\text{BET}}$ ) ( $\text{m}^2/\text{g}$ ), total pore volume (TPV) ( $\text{cc}/\text{g}$ ), and average pore size (TPS) (nm), for the investigated sample

Sample	$S_{\text{BET}}$ ( $\text{m}^2/\text{g}$ )	TPV ( $\text{cc}/\text{g}$ )	TPS (nm)
LFCO	30.889	0.0406	2.6281

radii, it is improbable for the investigated sample to exhibit long-range ordering of B-site cations. Therefore, it is anticipated that the B-site will contain a random mixture of  $\text{Fe}^{3+}$  and  $\text{Cr}^{3+}$  ions. Nevertheless, numerous attempts to create  $\text{La}_2\text{FeCrO}_6$  with an ordered DPV structure have been made.

The law of approach to saturation (LAS) is used to calculate the saturation magnetization ( $M_s$ ) [43] according to the following equation:

$$M = M_s \left( 1 - \frac{A}{H} - \frac{B}{H^2} \right) + \chi H \quad (7)$$

where  $M_s$  denotes the saturation magnetization of the domains per unit volume, “A” refers to a micro-stress-related constant, “B” denotes a constant that represents the contribution of magneto-crystalline anisotropy, and  $\chi H$  is the forced magnetization term. Figure 9b shows the law of approach to saturation (LAS) plot for the investigated sample. The  $M_s$  of the  $\text{La}_2\text{FeCrO}_6$  NPs is determined by

intercepting the straight line with the magnetization axis at  $1/H^2$  to approach zero.

The magnetic parameters such as coercivity ( $H_c$ ), saturation magnetization ( $M_s$ ), remnant magnetization ( $M_r$ ), squareness ( $M_r/M_s$ ), exchange bias ( $H_{\text{EB}}$ ), and magnetic moment ( $n_B$ ) are reported in Table 6.

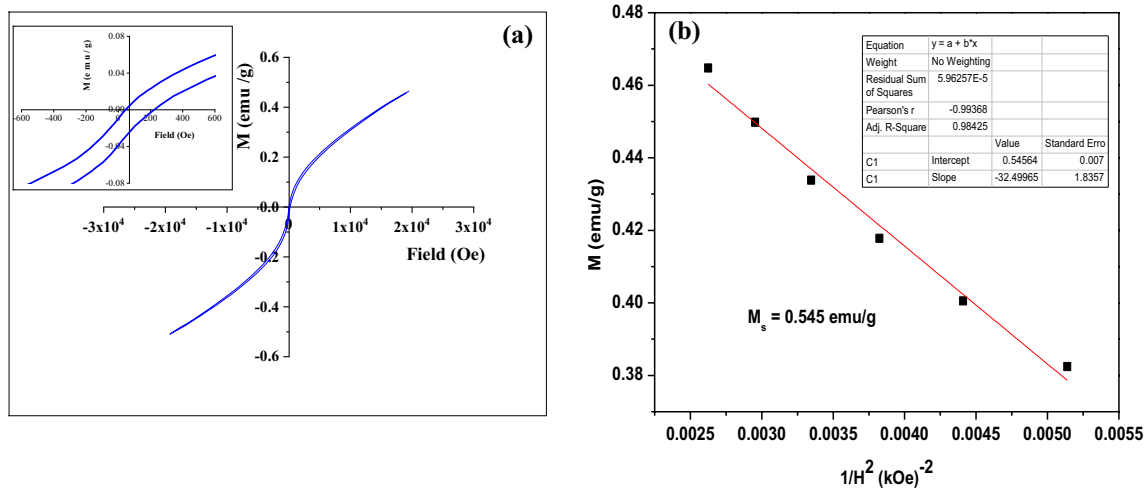
The experimental magnetic moment per unit cell ( $n_B$ ) is calculated from the  $M_s$  value using the following equation [44, 45]:

$$n_B = \frac{M_w \times M_s}{5585} \quad (8)$$

where  $M_w$  is the molecular weight of a particular ferrite composition.

The squareness ratio  $M_r/M_s$  can be used to determine the type of magnetic inter-grain exchange. It is less than 0.5, for the studied sample as reported in Table 5. Consequently, NPs interact magneto-statically [46, 47].

Based on the diamagnetic behavior of  $\text{La}^{3+}$  ions, the magnetic properties of perovskites are mainly originated from the magnetic interplay of spin states exhibited by the transition metal ions positioned in the B-site. In addition, the magnetic characteristics of LFCO sample depends not only on the magnetic coupling between  $\text{Fe}^{3+}$  and  $\text{Cr}^{3+}$  ions at the B-site, which can result in long-range ferromagnetic or anti-ferromagnetic order, but also on the way  $\text{Fe}^{3+}$  and  $\text{Cr}^{3+}$  ions

**Fig. 9** a and b The hysteresis loop, and b The law of approach to saturation (LAS) plot for of  $\text{La}_2\text{FeCrO}_6$  sample**Table 6** Saturation magnetization ( $M_s$ ), remnant magnetization ( $M_r$ ), coercivity ( $H_c$ ), energy loss, squareness ( $M_r/M_s$ ), anisotropy constant (K), and experimental magnetic moment  $n_B$  (exp)

$M_s$ (emu/g)	$M_r$ (emu/g)	$H_c$ (Oe)	Energy loss (erg/g)	$M_r/M_s$	K (emu.Oe/g)	$n_B$ (exp)
0.545	1.46E-02	134.25	313.66	0.029	76.215	0.042

are distributed at the B-site. This distribution can be fully ordered, partially ordered, or completely disordered, and is influenced by the differing  $d$ -orbitals and occupied states of the ions, including their  $t_{2g}$  or  $e_g$  orbitals and whether their orbital states are empty, half-filled, or fully filled. These factors also impact the ions' magnetic moments.

The  $\text{La}_2\text{FeCrO}_6$  sample displays a combination of anti-ferromagnetic (AFM), and ferromagnetic (FM) behavior, as depicted in Fig. 9a. According to the Kanamori–Goodenough (KG) rule [48, 49], there are three indirect-exchange interactions performed via the non-magnetic anion  $\text{O}^{2-}$  or, in other words, through the overlap between the  $2p$  orbital of oxygen and the  $d$  orbital of the transition metal ions  $\text{Fe}^{3+}$  ( $\text{Cr}^{3+}$ ).

These interactions can be detected as  $(\text{Fe}^{3+}-\text{O}^{2-}-\text{Fe}^{3+})$  or  $(\text{Cr}^{3+}-\text{O}^{2-}-\text{Cr}^{3+})$ , in addition to  $(\text{Fe}^{3+}-\text{O}^{2-}-\text{Cr}^{3+})$ . The irregular distribution of Cr and Fe ions at the B-sites leads to the occurrence of AFM behavior [50]. This feature is found to be predominant, as reported in the previous work [1–6]. The origin of the AFM behavior is the super-exchange interaction between  $\text{Fe}^{3+}$  and  $\text{Cr}^{3+}$  ions intermediated by  $\text{O}^{2-}$  [ $\text{Fe}^{3+}(\text{d}^5)-\text{O}-\text{Cr}^{3+}(\text{d}^3)$ ]. The obtained behavior is caused by the  $pd\pi$  hybridization between the  $e_g$  orbital of the transition metal and  $p\sigma$  orbital of the  $\text{O}_2$ , whereas FM is caused by  $pd\sigma$  hybridization.

Certainly, the  $pd\sigma$  hybridization is stronger than that of the  $pd\pi$ -type. But the number of excited-state configurations mediated by the  $pd\pi$  hybridization in the Fe–Cr pair is greater than that mediated by  $pd\sigma$  hybridization. Furthermore, among the  $pd\pi$  hybridization types, the LUMO ( $\epsilon_{\pi^-}^{\text{Fe}}$ ) and HOMO ( $\epsilon_{\pi^+}^{\text{Cr}}$ ) have the lowest energy contribution [7].

By taking these contributions into account, the magnetic character of the double perovskite  $\text{La}_2\text{FeCrO}_6$  is overwhelmed by the anti-ferromagnetic behavior accompanied by the existence of weak ferromagnetism. This trend was detected in other DPV oxides such as  $\text{La}_2\text{MMnO}_6$  ( $M = \text{Co}, \text{Ni}$ ) [51], and  $\text{Ho}_2\text{MMnO}_6$  ( $M = \text{Ni}, \text{Fe}, \text{Co}$ ) [52]. Figure 10

illustrates the microscopic mechanism of FM and AFM coupling between Fe and Cr.

The competition between the FM and AFM states asserts itself through the raised  $H_{\text{EB}}$  phenomenon observed in the MHL. This symmetry breaking phenomenon can be considered as a unidirectional anisotropy type.

The horizontal shift of the center of magnetic hysteresis from the zero field position ( $H=0$ ) is illustrated in the inset of Fig. 9a. This shift is due to the  $H_{\text{EB}}$ , which can be calculated according to the following relationship [46]:

$$H_{\text{EB}} = -(H_1 + H_2)/2 \quad (9)$$

The left and right coercivities are represented by  $H_1$  and  $H_2$  respectively. The  $H_{\text{EB}}$  is present in the sample as a result of the exchange coupling between the FM and the AFM components between  $\text{Fe}^{3+}$  and  $\text{Cr}^{3+}$  ions on B' and B'' sites [54].

The anisotropy constant ( $K$ ) is calculated according to the Stoner-Wohlfarth relation as given by the following Eq. (10):

$$K = \frac{H_c \times M_s}{0.96} \quad (10)$$

where  $H_c$  is the coercivity. The value of anisotropy constant ( $K$ ) is tabulated in Table 6.

Finally, the low magnetization is attributed to various factors, as previously mentioned, one of which is the disorder in the perovskite structure, which deviates from the ideal rock salt perovskite arrangement. The discrepant ionic radii of trivalent Cr and Fe pose a challenge to achieving an ordered phase, resulting in anti-site disorder where the regular Fe–Cr alternation is disrupted. Ateia et al. [36] prepared  $\text{La}_2\text{Fe}_2\text{O}_6$ , which has  $M_s$  and  $H_c$  equal to 1.060 emu/g and 304.63 Oe, respectively, while the values of  $M_s$  and  $H_c$  for the investigated sample  $\text{La}_2\text{FeCrO}_6$  are 0.545 emu/g and 134.25 Oe, respectively. This decrease is due to the replacement of  $\text{Cr}^{3+}$  ions with a small magnetic moment (3.87 BM) instead of  $\text{Fe}^{3+}$  ions with a large magnetic moment (5.916 BM).

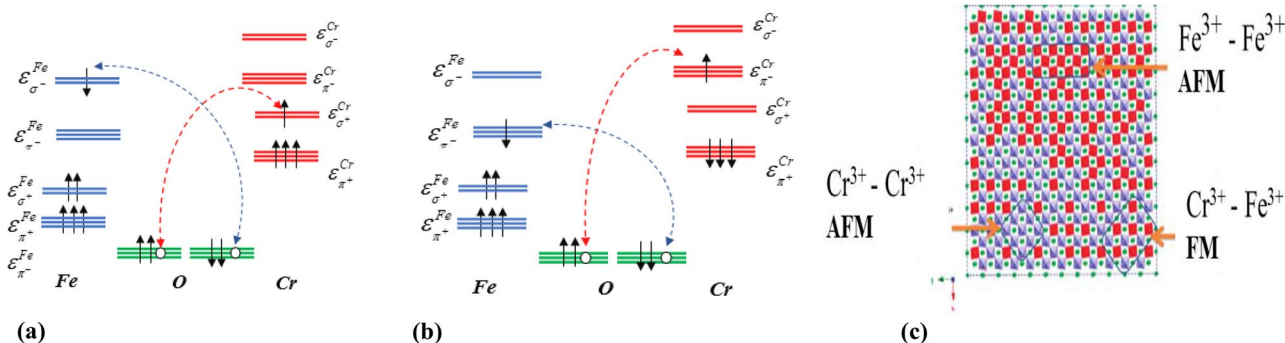


**Fig. 10** a–c The microscopic mechanism of FM and AFM coupling [7], and magnetic micro domains in  $\text{La}_2\text{FeCrO}_6$  materials, where  $\text{Fe}^{3+}$  and  $\text{Cr}^{3+}$  are located in the B and B' sites [53]

### 3.8 Heavy Metal Removal (Effect of Contact Time)

Ad-sorption is a chemical reaction that resembles a balanced reaction. When a solution comes into contact with a specific amount of ad-sorbent material, the concentration of the material adsorbed in the solution decreases until it reaches a state of equilibrium with the material on the ad-sorbent surface. When adsorption equilibrium is reached, the concentration of ad-sorbed material in the solution remains constant. Figure 11 shows the dependence of lead(II) ion removal on the contact time for  $\text{La}_2\text{FeCrO}_6$  NPs at a pH of 7. The effectiveness of removing  $\text{Pb}^{2+}$  improves as the duration of contact with  $\text{La}_2\text{FeCrO}_6$  increases, as a result

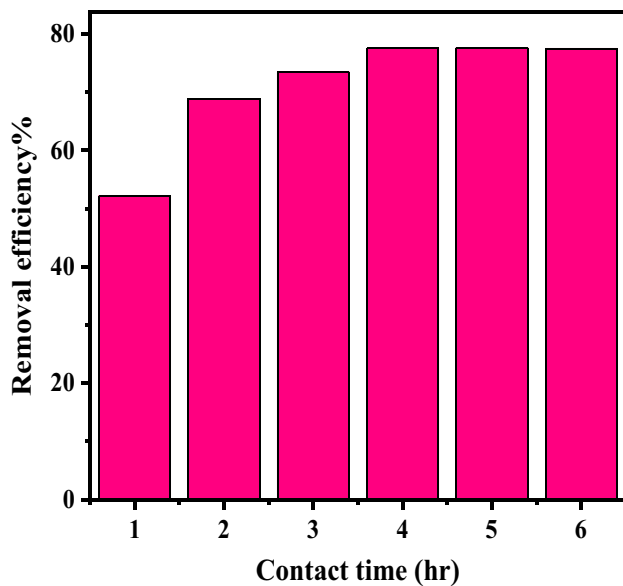


Fig. 11 Effect of contact time on the ad-sorption efficiency of  $\text{Pb}^{2+}$  ions

of  $\text{Pb}^{2+}$  being adsorbed onto active sites on the surface of the  $\text{La}_2\text{FeCrO}_6$ . The maximum  $\eta$  of  $\text{Pb}^{2+}$  is 77% at 5 h of contact time.

The porous nature and nano size of  $\text{La}_2\text{FeCrO}_6$  as illustrated in FESEM images increase the surface area, as well as the ad-sorption of  $\text{Pb}^{2+}$  on the ad-sorbent surface. According to the findings of this study, the DPV  $\text{La}_2\text{FeCrO}_6$  is an effective adsorbent for  $\text{Pb}^{2+}$  removal. The Langmuir and Freundlich ad-sorption models [20, 55, 56] are used to scrutinize the ad-sorption isotherms, with the following equations, respectively.

$$\frac{C_e}{q_e} = \frac{1}{q_m K_L} + \frac{C_e}{q_m} \quad (11)$$

$$\ln q_e = \ln K_f + \frac{1}{n} \ln C_e \quad (12)$$

where  $K_L$  denotes the Langmuir constant,  $K_f$  refers to the Freundlich constant and  $q_m$  is the ad-sorption capacity (mg/g). Figure 12a and b illustrates the fitting of  $\text{Pb}(\text{II})$  ad-sorption data onto  $\text{La}_2\text{FeCrO}_6$  using the previous isotherm models.

The correlation coefficient ( $R^2$ ) values for the Langmuir and Freundlich isotherms are 0.9898 and 0.9729, respectively, according to the inset table in Fig. 12.

Figure 12 shows that both models, along with the experimental data, are well fitted. The first model, considers the ad-sorption process of a monolayer of molecules on solid surfaces [57, 58]. Based on the data in Eq. 11 and Fig. 12a, the maximum ad-sorption capacity is calculated to be 17.36 mg per gram. The  $K_L$ , equals  $0.21 \text{ L mg}^{-1}$  which designates high sorption energy between  $\text{Pb}(\text{II})$  and  $\text{La}_2\text{FeCrO}_6$ . On the other side, in the Freundlich model,  $K_f$  and  $1/n$  are determined from the intercept and slope of Fig. 12b. The

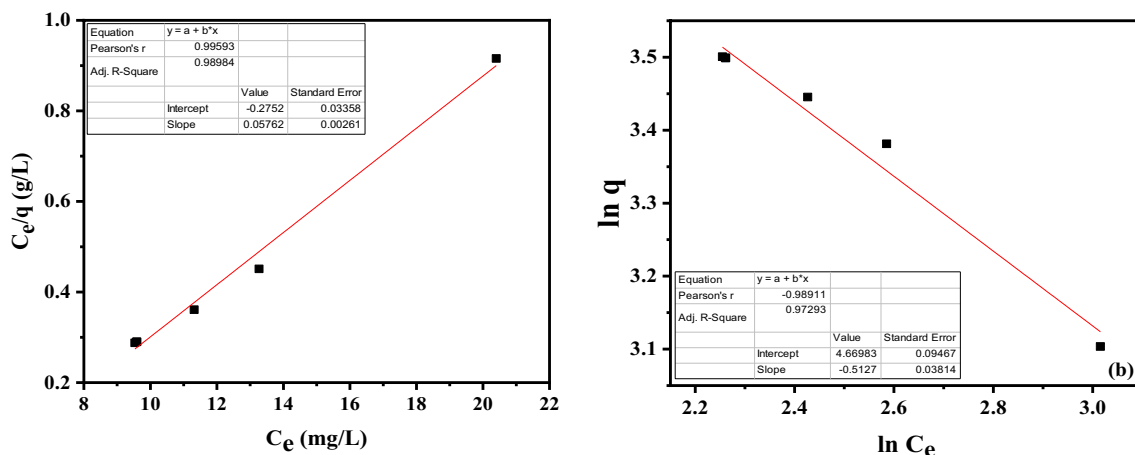


Fig. 12 Linear fit of experimental data of the ad-sorption of  $\text{Pb}^{2+}$  onto  $\text{La}_2\text{FeCrO}_6$

low value of  $1/n$  (0.511) confirms that Pb(II) ad-sorption on  $\text{La}_2\text{FeCrO}_6$  is favorable. The electrostatic nature of the bonding between Pb(II) and the  $\text{La}_2\text{FeCrO}_6$  nano ferrite sample is thought to be the main cause of the observed high sorption of  $\text{La}_2\text{FeCrO}_6$  to the Pb(II) ion.

## 4 Conclusion

The double perovskite  $\text{La}_2\text{FeCrO}_6$  was synthesized in nano-phase by the citrate auto-combustion technique. The structure, morphology, and magnetic properties have been studied. XRD of the sample at 300 K shows that  $\text{La}_2\text{FeCrO}_6$  is crystallized in the orthorhombic phase with a crystallite size of 22.6 nm. The sample has a sponge-like morphology with clear pores. EDAX mapping illustrated the uniform distribution of constituent elements in the sample. The sample  $\text{La}_2\text{FeCrO}_6$  has antiferromagnetic behavior with a weak ferromagnetic contribution. The significant exchange bias found in the study of  $\text{La}_2\text{FeCrO}_6$  provides strong support for the connection between its ferromagnetic (FM) and antiferromagnetic (AFM) components, which attributed to the presence of  $\text{Fe}^{3+}$  and  $\text{Cr}^{3+}$  ions in the B' and B'' sites. The maximum removal efficiency of  $\text{Pb}^{2+}$  is 77% at 5 h of contact time. The Langmuir and Freundlich isotherm models are the best descriptions of the ad-sorption isotherm of  $\text{Pb}^{2+}$  ions.

**Author Contributions** EEA involved in the development of the concept, validation process, preparation of the first draft, review and editing of the final manuscript, creation of visual aids, and provided oversight. MMA participated in preparing materials, organizing analyzing data, performing formal analysis and investigation, verifying results, creating visual representations, and reviewing and editing the final manuscript. DG participated in material preparation, data collection and analysis, formal analysis, investigation, selection of optimal material parameters, development of methodology, writing the initial draft, validation, visualization, as well as review and editing. MM contributed to the part involving X-ray diffraction analysis, and reviewing the final manuscript.

**Funding** Open access funding provided by The Science, Technology & Innovation Funding Authority (STDF) in cooperation with The Egyptian Knowledge Bank (EKB). This research did not receive any specific grants from funding agencies in the public, commercial, or not-for-profit sectors.

**Data Availability** Data is available under request.

## Declarations

**Conflict of interest** The authors declare that they have no known competing financial interests or personal relationships that could have appeared to influence the work reported in this paper.

**Open Access** This article is licensed under a Creative Commons Attribution 4.0 International License, which permits use, sharing, adaptation, distribution and reproduction in any medium or format, as long

as you give appropriate credit to the original author(s) and the source, provide a link to the Creative Commons licence, and indicate if changes were made. The images or other third party material in this article are included in the article's Creative Commons licence, unless indicated otherwise in a credit line to the material. If material is not included in the article's Creative Commons licence and your intended use is not permitted by statutory regulation or exceeds the permitted use, you will need to obtain permission directly from the copyright holder. To view a copy of this licence, visit <http://creativecommons.org/licenses/by/4.0/>.

## References

1. W.E. Pickett, Phys. Rev. B **57**, 10613 (1998)
2. H.-T. Jeng, G.Y. Guo, Phys. Rev. B **67**, 094438 (2003)
3. D.P. Rai, A. Shankar, M.P. Ghimire, R.K. Sandeep, Comput. Mater. Sci. **101**, 313 (2015)
4. B. Gray, N.L. Ho, J. Liu, J. Chakhalian, J.W. Freeland, Appl. Phys. Lett. **97**, 013105 (2010)
5. C.M. Bonilla, D.A. Landinez Tellez, J. Arbey, A. Rodríguez, E. Vera López, J. Roa-Rojas, Physica B **398**, 208 (2007)
6. Y. Zhang, V. Ji, K.-W. Xu, Mater. Chem. Phys. **136**, 570 (2012)
7. M. Fiebig, J. Phys. D **38**, R123 (2005)
8. J.F. Scott, Nat. Mater. **6**, 256 (2007)
9. S. Idrissi, R. Khalladi, S. Mtougui, S. Ziti, H. Labrim, I. ElHousni, N. ElMekkaoui, L. Bahmad, J. Electron. Mater. **527**, 121406 (2019)
10. K.I. Kobayashi, T. Kimura, H. Sawada, K. Terakura, Y. Tokura, Nature **395**, 677–680 (1998)
11. W.E. Pickett, D.J. Singh, Phys. Rev. B **53**, 1146 (1996)
12. S. Vasala, Progr. Solid State Chem. **43**, 1–36 (2015)
13. E. Abdul Rahman Assirey, SPJ **27**, 817–829 (2019)
14. F.S. Galasso, F.C. Douglas, R.J. Kasper, J. Chem. Phys. **44**, 1672 (1966)
15. E.E. Ateia, A.T. Mohamed, H. Elshimy, Appl. Nanosci. **10**, 1489–1499 (2020)
16. A.W. Sleight, J.F. Weiher, J. Phys. Chem. Solids **33**, 679–687 (1972)
17. K. Miura, K. Terakura, Phys. Rev. B **63**, 104402 (2001)
18. K.-I. Kobayashi, T. Kimura, Y. Tomioka, H. Sawada, K. Terakura, Y. Tokura, Phys. Rev. B **59**, 11159 (1999)
19. F. Schüth, K.S.W. Sing, J. Weitkamp, *Handbook of Porous Solids*, vol. 1 (Wiley, Hoboken, 2002), pp.250–275
20. M.M. Arman, A.A.R. Gamal, Appl. Phys. A **129**(5), 331 (2023)
21. M.A. Malana, R.B. Qureshi, M.N. Ashiq, M.F. Ehsan, Ceram. Int. **42**, 2686–2692 (2016)
22. M.M. Arman, M.A. Ahmed, Appl. Phys. A **128**(7), 1–9 (2022)
23. M.H.K. Rubel, T. Takei, N. Kumada, M.M. Ali, A. Miura, K. Tadanaga, M. Avdeev, Chem. Mater. **28**(2), 459–465 (2016)
24. M.T. Anderson, K.B. Greenwood, G.A. Taylor, K.R. Poepelmeier, Progr. Solid State Chem. **22**, 197–233 (1993)
25. E.E. Ateia, H. Ismail, H. Elshimy, M.K. Abdelmaksoud, J. Inorg. Organomet. Polym. Mater. **31**, 1713 (2021)
26. M.A. Ahmed, N.G. Imam, M.K. Abdelmaksoud, Y.A. Saeid, Magnetic transitions and butterfly-shaped hysteresis of Sm–Fe–Al-based perovskite-type orthoferrite. J. Rare Earths. **33**, 965–971 (2015)
27. M.A. Amer, A. Matsuda, G. Kawamura, R. El-Shater, T. Meaz, F. Fakhry, J. Alloys Compd. **735**, 975 (2018)
28. E.E. Ateia, S. Hussien, A.T. Mohamed, J. Inorg. Organomet. Polym. **33**, 216–227 (2022)
29. M.A. Amer, T.M. Meaz, S.S. Attalah, A.I. Ghoneim, J. Alloys Compd. **654**, 45e5546 (2016)
30. N. Jahan, A.K.M. Zakaria, Mater. Sci.-Pol. **34**(1), 185–191 (2016)

31. Y.T. Prabhu, K.V. Rao, *World J. Nano Sci. Eng.* **4**, 21–28 (2014)
32. D. Nath, F. Singh, *Mater. Chem. Phys.* **239**, 122021 (2020)
33. M.A. Gabal, Y.M. Angari, A.Y. Obaid, A. Qusti, *Adv. Powder Technol.* **25**, 457–461 (2014)
34. M.A. Ateia, M.G. Fayed, S. El-Hout, S.G. Mohamed, M.M. Arman, *Appl. Phys. A* **128**(6), 1–10 (2022)
35. M.D.I. Bhuyan, S. Das, M.A. Basith, *J. Alloys Compd.* **878**, 160389 (2021)
36. E.E. Ateia, A.T. Mohamed, *J. Mater. Sci.* **31**, 19355–19365 (2020)
37. D.N. Singh et al., *Physica B* **550**, 400–406 (2018)
38. Y. Wang, L. Zhang, S. Ma, Y. Zhao, D. Tan, B. Chen, *Appl. Phys. Lett.* **118**, 231903 (2021)
39. M. Nasir, S. Kumar, N. Patra, D. Bhattachary, S. Nath Jha, D.R. Basaula, S. Bhatt, M. Khan, S. Wei Liu, S. Biring, S. Sen, *ACS Appl. Electron. Mater.* **1**, 141–153 (2019)
40. F. Liu et al., *J. Alloys Compd.* **773**, 511–518 (2019)
41. J. Fu et al., *Int. J. Miner. Metall.* **25**, 950 (2018)
42. M. N. Kajama, N. C. Nwogu & E. Gobina, *WIT Trans. Ecol. Environ.* **193** (2015).
43. M.M. Arman, *Appl. Phys. A* **128**(12), 1103 (2022)
44. E.E. Ateia, A.T. Mohamed, *J. Magn. Magn. Mater.* **426**, 217–224 (2017)
45. E.E. Ateia, Y.A. Saeid, M.K. Abdelmaksoud, *J. Supercond. Nov. Magn.* (2023).
46. E.E. Ateia, M.M. Arman, A.T. Mohamed, *Sci. Rep.* **13**, 3141 (2023)
47. E.E. Ateia, B. Hussein, C. Singh, M.M. Arman, *Eur. Phys. J. Plus* **137**(4), 1–11 (2022)
48. J. Kanamori, *J. Phys. Chem. Solids* **10**, 87–98 (1959)
49. J.B. Goodenough, *Phys. Rev.* **100**, 564–573 (1955)
50. L. Yuan, K. Huang, C. Hou, W. Feng, S. Wang, C. Zhou, S. Feng, *New J. Chem.* **38**, 1168–1172 (2014)
51. M. Ullah et al., *J. Magn. Magn. Mater.* **377**, 197–203 (2015)
52. K.P. Shinde et al., *J. Magn. Magn. Mater.* **544**, 168666 (2022)
53. M.E. Castrejón, M. Guaderrama, L. Fuentes, J. Prado-Gonjal, A.M. González, M.A. Rubia, E. Morán, *Inorg. Chem.* **50**, 8340 (2011)
54. M.M. Arman, M.A. Ahmed, S.I. El-Dek, *J. Supercond. Nov. Magn.* **31**, 1867–1879 (2018)
55. Q. Liu, Y. Liu, *J. Colloid Interface Sci.* **268**(1), 266–269 (2003)
56. E.E. Ateia, A.T. Mohamed, *J. Inorg. Organomet. Polym. Mater.* **32**, 1389–1399 (2022)
57. E.E. Ateia, K. Elsayed, D.E. El-Nashar, *Appl. Phys. A* **129**, 118 (2023)
58. E.E. Ateia, A.T. Mohamed, M. Morsy, *Metal Oxide-Carbon Hybrid Materials* (Elsevier, Amsterdam, 2022)

**Publisher's Note** Springer Nature remains neutral with regard to jurisdictional claims in published maps and institutional affiliations.